PAPER

Check for updates

Analysis and optimization of alloyed Al-p$^+$ region and rear contacts for highly efficient industrial n-type silicon solar cells

Yi Wei, [ID] *[a] Xue Jiang, [ID] [a] Yiren Lin,[a] Xichuan Yang, [ID] [b] Guohui Li,[c] Xuyang Liu,[a] Ping Li[a] and Aimin Liu[a]

This paper aims to develop high quality screen-printed Al emitters and improve the interface condition of rear contacts in industrial silicon solar cells. We propose to introduce an ultra-thin SiO_2 buffer layer between the silicon bulk and metal contact during the fabrication process. A post-annealing strategy is adapted to further modify the Al doping profiles. The experimental results show that the effects of this oxide layer on migrating the nonuniformity of Al-p$^+$ region and decreasing the defects at the metal–silicon interface are significant. The recombination velocity of contacts, which is extracted from the measured S_{rear} by an analytical model, exhibits a decrease by 90.8% and the series resistance is reduced by 60.3% for the improved contacts compared to the conventional screen-printed contacts. Finally, this technique is applied to large-area (156 × 156 mm^2) industrial n-type silicon solar cells and leads to a 2.18% increase in average cell efficiency, including a 12.82 mV increase in open-circuit voltage V_{oc} and 0.99 mA cm^{-2} increase in short-circuit current density J_{sc} compared with solar cells fabricated by a standard industrial process. A 19.16% efficient cell with a V_{oc} of 637.47 mV is achieved.

1 Introduction

Recently, n-type silicon solar cells have received increased attention for industrial applications, such as the n-type rear-junction Passivated Emitter Rear Totally-diffused (PERT) solar cells.[1–3] However, laser ablation and high-temperature boron diffusion techniques (∼1000 °C) are necessary in the fabrication process of PERT solar cells, which inevitably increases the damage and heat induced defects, as well as the fabrication cost. To achieve a more simplified and cost-efficient process while still being able to reach high efficiency, a screen-printing method is increasingly used in industrial crystalline cells.[4,5] The Al-p$^+$ region, which is alloyed from Al pastes, provides an ohmic contact and is commonly used as an emitter in new concept n-type cells, such as the n$^+$np$^+$ front-contact cells[6–10] and the interdigitated back contact (IBC) cells.[11,12] Recent publications have indicated that the electrical properties of the Al-p$^+$ region and contacts significantly influence the cell performance and are considerably affected by the fabricating conditions. In the

industrial alloying process, the screen-printing Al-paste is fired in a belt furnace with peak temperatures at about 800 °C to 900 °C.[13] Si starts to melt into Al at 660 °C and forms an Al–Si liquid state. It recrystallizes again during cooling, while some Al atoms remain in the Si crystal lattice and form the Al-p$^+$ region.[14–16] Generally, the re-solidification is complete within several seconds and is assumed to be under non-thermal–equilibrium conditions; such a quick formation process usually introduces agglomerations and voids at the interface of Si–Al in industrial solar cells. Furthermore, the alloying reaction starts locally at the contacting points between Al and Si, and forms local Si–Al liquid melt on the wafer surface, which causes thickness inhomogeneities in the Al-p$^+$ region. These disadvantageous effects strongly influence the field effect of the p–n junction and the ohmic contact. It is known that applying a thicker paste and increasing the alloying temperature can mitigate the thickness inhomogeneity.[17,18] Nevertheless, a thicker paste usually aggravates wafer bow due to the contrast of thermal expansion coefficients between Si material and Al paste matrix after firing. Moreover, Al–O defect centers are inevitably introduced due to high temperature treatment,[19] which leads to the decrease of carrier lifetime in devices. Therefore, the uniformity control and the understanding of the recombination in Al-emitters are of prime importance for solar cell design strategies and process optimization.

The aim of this paper is to improve the electrical properties of Al-p$^+$ layer and the interface condition of rear contacts in n-type silicon solar cells. We focus on their formation process

[a]School of Physics and Optoelectronic Engineering, Dalian University of Technology, Dalian 116024, China. E-mail: ywei@dlut.edu.cn

[b]State Key Laboratory of Fine Chemicals, Institute of Artificial Photosynthesis, DUT-KTH Joint Education and Research Centre on Molecular Devices, Dalian University of Technology, Dalian 116024, Liaoning, China

[c]Key Laboratory of Advanced Transducers and Intelligent Control Systems, Ministry of Education and Shanxi Province, College of Physics and Optoelectronics, Taiyuan University of Technology, No. 79 Yingze Street, Taiyuan, 030024, China

and develop an industrially applicable method to integrate an ultra-thin SiO_2 buffer layer at the Si–Al interface. To determine the contact recombination velocities of the Al-alloyed rear contacts, area-averaged carrier lifetimes measured by the microwave-detected photoconductance decay (MWPCD) technique are analyzed.[20] In contrast to the typical industrial fabricating process, the beneficial effects of such a thin layer on mitigating the nonuniformity of the Al-p$^+$ region and decreasing the defects at the metal–silicon interface are presented. Finally, large-area (156 × 156 mm^2) industrial n-type Si solar cells featuring full-area and improved Al rear emitters are fabricated.

2 Experimental details

All the samples in this study were prepared on (100)-oriented Czochralski (Cz) n-type silicon wafers of 1–3 Ω·cm resistivity, with a thickness of 200 μm. After RCA cleaning followed by a HF dip, the test samples for SEM and ECV measurements were polished with a special solution. The Al-p$^+$ region is formed by firing the screen-printed Al pastes in an industrial conveyor belt furnace. The samples for Quasi-Steady-State Photoconductance (QSSPC) lifetime measurements are silicon samples with pyramidally textured/polished front surface and passivated with SiN$_x$. The lifetime of the starting wafers (bare n-type silicon, 52 × 52 mm) are about 1.9 μs. The rear surface is Al screen-printed, and is fired under industrial conditions. The residual Al paste and the Al–Si eutectic on ECV and QSSPC samples are finally removed in a boiling 37% solution of HCl. For the studies on solar cells, we fabricate cells in two groups for comparison. The group 1 cells are fabricated by a standard industrial process. In group 2, the cells are with an interfacial oxide layer. The fabrication flow chart is demonstrated in Fig. 1. The cells are all of front Ag contact back-junction structure, with SiN$_x$ front surface field (FSF) passivation, processed on 156 × 156 mm^2 wafers. After industrial texturing and RCA cleaning, we perform an n$^+$ FSF phosphorus diffusion on the textured front surface, resulting in a FSF sheet resistance of 59 Ω sq^{-1}. The phosphorus silicate glass (PSG) is subsequently etched off in HF solution. To form a polished rear surface, we performed a single side wet chemical etch of about 3 μm. The oxide thin layers are grown from thermal oxidation at 860 °C on both sides of the samples, and then washed off from the front surface by HF solution. This SiO_2 layer is estimated to be 1.86 nm by ellipsometry measurement. Afterwards, an 80 nm-thick SiN$_x$ layer with a refractive index $n = 2.0$ is deposited on the front side of the wafers by an in-line microwave Plasma Enhanced Chemical Vapor Deposition (PECVD) system. A conventional grid pattern
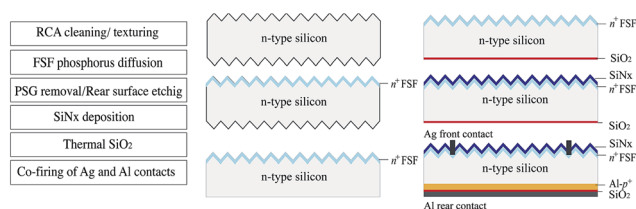
on the front and a full area pattern on the rear are screen-printed by using Ag and Al pastes, respectively. The Al-p$^+$ emitters and the contacts are formed in an infrared conveyor belt furnace by a co-firing process at 880 °C for 13 s. In order to characterize the surface recombination velocity of metallized rear surfaces, lifetime measurements were performed by MWPCD measurements. The wafers were cleaned and polished in a wet chemical process. We defined 23 contact geometry with an area of 25 × 25 mm on each 156 × 156 mm^2 wafer. The geometries vary in contact pitch p (ranging from 300 to 3500 μm) and contact width a (ranging from 80 to 500 μm). We completed the contact formation by full-area screen printing Al paste at approximately 880 °C and finally an 80 nm-thick SiN$_x$ layer was deposited on both sides of the wafers by PECVD.

3 Results and discussion

3.1 Influence on the formation of the homogeneous Al-p$^+$ layer

(i) Formation of Al-p$^+$ region. The Al-emitter is generally formed in a belt furnace with peak temperatures around 800 °C to 900 °C in the contact firing step of solar cell fabrication. Fig. 2 shows the formation process of Al-p$^+$ regions and the rear contact from a screen-printed aluminium paste. After the burn-out of the organic components in the pastes, the alloying process starts with the melting of the Al at 660 °C. The liquid aluminium locally penetrates the shells of the Al particles to make contact with the silicon surface to start the melt with Si, and to neighbouring Al particles. It is important to notice that the Al paste particles are held in place by the matrix during the whole firing process and the transport of the liquid Si–Al takes place from particle to particle *via* small sintering necks.[14] The alloying reaction thus starts locally on the wafer surface, leading to the formation of liquid "lakes" on the wafer surface, as demonstrated in Fig. 2(b). According to the formation model of M. Rauer,[17] when the Al–Si melt on the surface exceeds a critical thickness, it starts to contract to minimize the interface tension between Al–Si liquid and solid Si wafer, leading to melt accumulation and depletion. On cooling down, silicon is rejected from the melt and recrystallizes epitaxially on the wafer surface. As the accumulated regions effectively provide a higher amount of Al–Si melt, the Al-p$^+$ region growth is enhanced
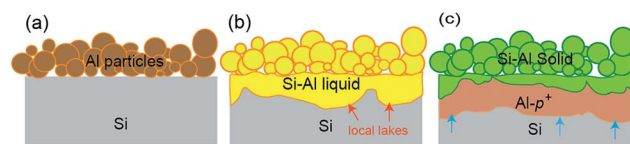

Fig. 2 Sketch of the formation of Al-p$^+$ regions and rear contact from a screen printed aluminium paste. (a) After drying (removal of solvents) a porous paste matrix of aluminium particles is attached to the Si wafer surface. (b) The alloying process starts with the melting of the aluminium at 660 °C. The liquid aluminium dissolves silicon, forming local Si–Al liquid "lakes" on the wafer surface. (c) On cooling down after reaching the eutectic temperature of 577 °C, an Si–Al solid layer is present on top of the Al-p$^+$ region. Arrows indicate the enhanced thickness due to locally accumulated Si–Al liquid.

Fig. 1 Process flow of the solar cells in group 2.

within these regions. The residual Al–Si melt solidifies at the eutectic temperature of 577 °C, building a compact Al–Si layer of eutectic composition on top of the Al-p$^+$ region, as shown in the sketch in Fig. 2(c). This model explains the formation of lateral thickness inhomogeneities in the Al-p$^+$ region.

(ii) Thickness homogeneity. The thickness of the Al-p$^+$ layer is determined by the amount of Si dissolved into the Al–Si melt at the peak temperature. Theoretical calculations reveal that increasing the thickness of the deposited Al pastes or peak alloying temperature can improve the quality of the Al-p$^+$ region. However, high temperatures tend to degrade the Al emitter quality as a result of nonuniformity triggered by the agglomeration of Al–Si melt in combination with the bandgap narrowing due to the high doping effect. Moreover, it is found that the critical temperature above which the solar cell performance starts to degenerate is lower for thicker Al layers, which puts a limit on the maximum thickness that can be achieved.[21]

Since the liquid Al transports through sintering necks between paste particles to make contact with Si, the locally started reaction between Si and Al can not make full coverage of the surface. Therefore, the morphology of the Si surface, as well as the presence of an interface layer becomes important to the homogeneity of the Al-p$^+$ layer. In Fig. 3, scanning electron microscope (SEM) images of the cross section of the Al-doped p$^+$ regions realized from different surface conditions are shown. Due to the potential contrast between the Al-p$^+$ region and the Si base, the Al-p$^+$ regions are clearly visible.

In order to compare the influence of the surface morphology and the SiO$_2$ interface layer on homogeneity, the thickness distributions of the Al-p$^+$ region cross-section are measured.[22] Fig. 3(a) shows a discontinuous alloy layer at the Si–Al interface for the pyramidally textured sample. The tops of the pyramidal structures on the rear surface are completely melted, some bottom parts inadequately contact with the Al paste which results in an average thickness of 3.46 μm and full width at half maximum (FWHM) of 1.37 μm in the Gaussian fitted profile, as shown in the graph below the image. This situation can be improved using a polished surface as shown in Fig. 3(b), the alloy layer is more continuous whereas the interface is still rough with abrupt tips and occasional cracks. The average

thickness is 3.76 μm and FWHM is 0.76 μm. In Fig. 3(c), we apply a thin SiO$_2$ layer on the polished Si surface before screen-printing. It is clearly seen that the Si–Al alloy layer exhibits more smooth and uniform properties. The average thickness is 3.67 μm and FWHM is reduced to 0.39 μm, a remarkable effect on homogeneity is observed. It is believed that the SiO$_2$ layer works as a buffer, which slows down the immediate contact between Al particles in the paste and Si surface during the firing process. This effect thus reduces the large amount of melt at the agglomerated regions, resulting in a more uniform Al-p$^+$ layer over a wide range.

3.2 Influence of the post-annealing conditions

(i) Influence on Al diffusion profiles. Due to the fact that the Al-p$^+$ regions placed on the rear side of a solar cell work as a p–n junction in n-type back-junction solar cells, the diffusion depth and doping level of Al are essential to form a reasonable electrical field to separate the charge carriers and enable diffusion of minority carriers. In order to modify the Al diffusion profile and improve the performance of solar cells, we adopt a post-annealing strategy after the firing process. Five Al doped silicon samples under different diffusion conditions are prepared to determine the influence of different doping levels, and the thickness of the Al-p$^+$ region. The post-annealing treatments are kept at 400 °C, 450 °C, 500 °C, 550 °C and 600 °C in ambient air, the annealing time is 20 min. The peak concentration N_{peak} and its corresponding depth position d_{peak} are extracted from the Al doping profile curves of Fig. 4(a). As seen in Fig. 4(b), the annealing treatments provide higher doping levels and thicker Al-p$^+$ layer depths. As the temperature rises to 550 °C and above, it seems that the Al doping concentration reaches a maximum value and maintains a constant level as the annealing temperature rises, while the junction depths increase further. Al bumps begin to be observed at screen-printed surfaces at 600 °C. It is suspected that the driving force for the agglomeration is to reduce the interface energy between the Al–Si melt and Si by minimizing the contact interface area. This occurs by the
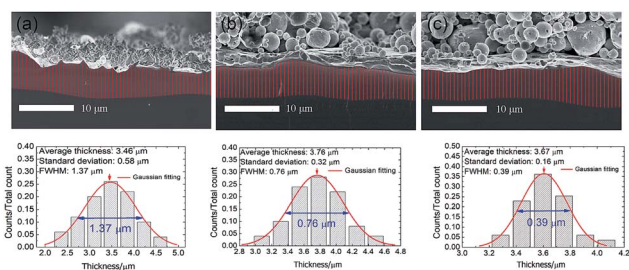

Fig. 3 SEM images of the cross-section of Al-doped p$^+$ regions at Si surfaces. The samples are of (a) a pyramidally textured Si surface, (b) a polished Si surface, (c) a polished and oxidized Si surface. All the three samples are fired at the same industrial condition of 880 °C. Direct measurements of the Al-p$^+$ region thickness are performed, as marked red for (a)–(c). A Gaussian distribution is fitted to each measured result, as shown below the images.
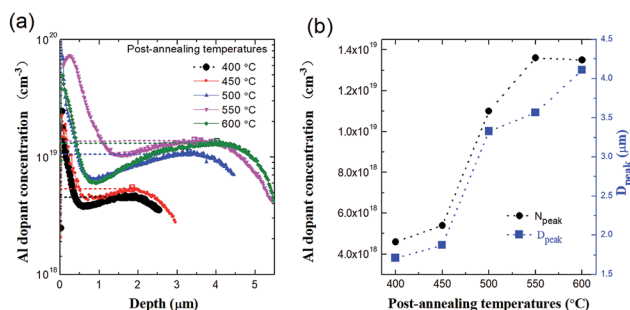

Fig. 4 (a) Al doping profiles of silicon samples under different post-annealing temperatures. (b) The peak doping concentration of Al as a function of post-annealing temperatures. All samples are screen-printed with industrial Al pastes and fired in an infrared conveyor belt furnace at 880 °C for 13 s. The post-annealing temperature is varied from 400 °C to 600 °C for 20 min.

formation of a higher contact angle, which produces the bumps.[21]

(ii) Influence on effective lifetime. In order to determine the influence of post-annealing on effective lifetime (τ_{eff}), injection-dependent lifetime measurements were performed by the QSSPC technique.[23,24] The implied open-circuit voltage iV_{oc} at one sun is used to determine the voltage of the device if contacts were applied, when only the recombination of the investigated emitter is considered. In Fig. 5(a) and (b), the τ_{eff} values and iV_{oc} at 1 sun are plotted as a function of the post-annealing temperature. The improvement in lifetime is quite clear, the τ_{eff} curves for samples which suffer a post-annealing treatment are higher than those of the samples without annealing, as shown by the red, magenta, green and blue curves. The lifetime values can be gradually boosted as the annealing temperature increases from 200 °C to 500 °C. The corresponding lifetime values have been extracted from Fig. 5(a), as shown by the right axis in Fig. 5(b). A similar trend is also observed from the annealing condition dependent iV_{oc} curves, which exhibit a high value of 675 mV at the annealing temperature of 500 °C.

To further investigate the influence of the annealing condition on τ_{eff} and find an optimal condition for solar cell treatment, a more meticulous work was performed with a set of samples which were annealed at various temperatures and times. The test samples are of n-type silicon with polished and passivated front surface, and Al-p$^+$ back surface field. The QSSPC measurements were performed at an injection level of 10^{15} cm^{-3}. As shown in the three-dimensional diagram of Fig. 6, the annealing conditions varied from 400 to 600 °C, for 10 to 60 min. It can be seen that the τ_{eff} of the samples increased with the annealing time at 400 °C. When annealed at 500 °C, the τ_{eff} reached the highest value at an annealing time of 30 min and then began to decline as the time increased to 45 and 60 min. For this same annealing time, the τ_{eff} of the sample annealed at 500 °C was greater than that of the sample annealed at 400 °C. However, when the annealing temperature reached 600 °C, the τ_{eff} of the samples clearly decreased. And with the increase of annealing time, the τ_{eff} tended to be lower. This is because the Al bumps are greatly enhanced at 600 °C,
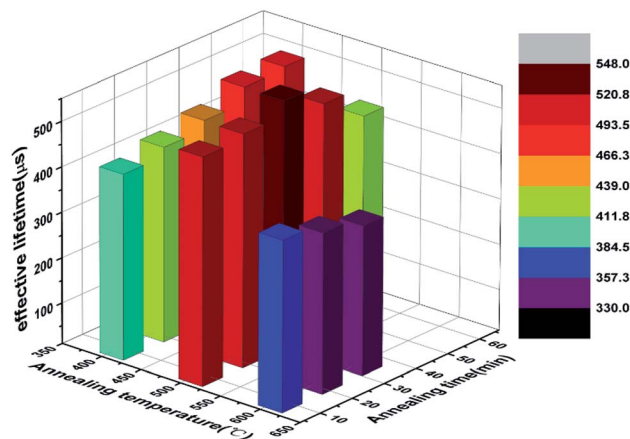

Fig. 6 Measured effective minority carrier lifetimes for samples annealed at different conditions. The temperatures are varied from 400 to 600 °C, for 10 to 60 min. The injection level is maintained at 10^{15} cm^{-3}.

forming a large number of surface defects and locally high-doped regions, resulting in an increase of surface recombination and Auger recombination. Considering that prolonged annealing can cause agglomeration and damage to the sample, the longer the annealing time is, the more defects will be generated, we thus chose 500 °C for 30 min as the optimum annealing conditions.

3.3 Recombination in Al-p$^+$ region

The saturation current densities of the Al-p$^+$ regions ($j_{0,Al}$) can be experimentally determined *via* the QSSPC measurements. Under high-level injection conditions, the recombination rate in the Al-p$^+$ region has a quadratic dependence on the carrier density, as expressed in eqn (1)[25,26]

$$\frac{1}{\tau_{eff}(\Delta n)} - \frac{1}{\tau_{Auger}} = \frac{1}{\tau_{SRH}(\Delta n)} + \frac{1}{q n_i^2 W} \cdot j_{0,total} \cdot \Delta n, \quad (1)$$

where τ_{SRH} is the bulk Shockley–Read–Hall (SRH) lifetime, τ_{Auger} is the bulk Auger lifetime, $j_{0,total}$ is the total saturation current density, q is the elementary charge, n_i is the intrinsic carrier density, Δn is the excess carrier concentration, and W is the wafer thickness. According to the slope method,[27,28] the $\frac{1}{\tau_{eff}} - \frac{1}{\tau_{Auger}}$ curve shows a linear dependence of Δn, which can be used to extract $j_{0,total}$. For our asymmetric samples, the saturation current density of the Al emitter ($j_{0,Al}$) can be extracted by $j_{0,Al} = j_{0,total} - j_{0,residual}$. The saturation current density of samples without Al-p$^+$ region ($j_{0,residual}$) can be determined with the help of an additional symmetric reference. The $j_{0,Al}$ for the sample with SiO$_2$ and treated under 500 °C for 30 min is found to be 209.5 $\pm$ 44.5 fA cm^{-2}, exhibiting a marked decrease of 1.54 pA cm^{-2} compared with the standard processed sample.

For n-type Si solar cells where the Al-p$^+$ regions act as rear emitters, the thicknesses of the Al-p$^+$ regions directly affect the screening of electrons from the metallized, recombination-active rear surfaces. Therefore, it influences the open-circuit
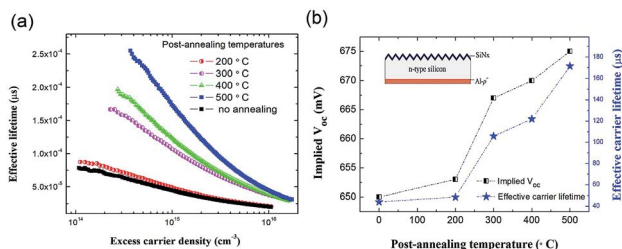

Fig. 5 (a) Measured injection dependent effective minority carrier lifetime for pyramidally textured samples with different post-annealing conditions. (b) Implied V_{oc} and effective carrier lifetime as a function of the post-annealing temperature. The injection level is kept at 10^{15} cm^{-3}. The structure of the test samples is sketched in the inserted graph. The drawn dot dash lines are guides to the eye.
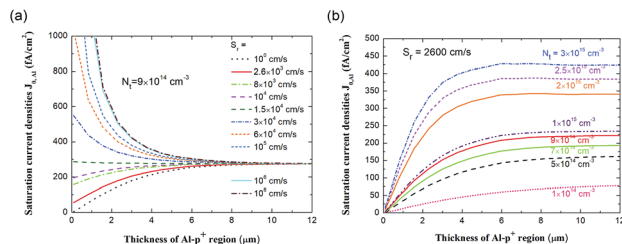
Paper

Fig. 7 Simulated results of saturation current densities of Al emitter as a function of doping depth. The sample structure is of SiN$_x$ passivated front surface and the rear surface is Al screen-printed, as shown in the inset of Fig. 5(b). The doping profile at 500 °C in Fig. 4(a) is used for simulations. The SRH recombination, the Auger recombination, and the effect of incomplete ionization of Al acceptors are considered in the simulation model. (a) The S_r is varied from 10^0 to 10^8 cm s^{-1} and the N_t is 9×10^{14} cm^{-3}. (b) The influence of the defect density, N_t is varied from 1×10^{14} cm^{-3} to 3×10^{15} cm^{-3} and S_r is 2600 cm s^{-1}.
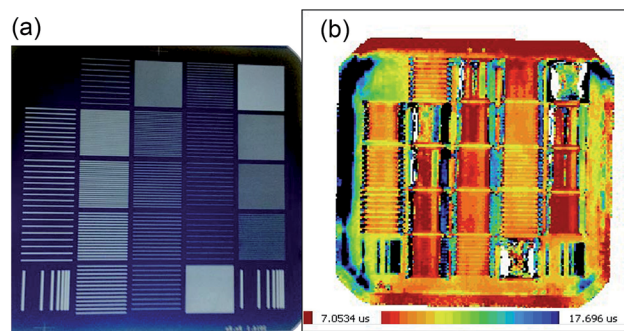

Fig. 8 (a) Image of test sample for the measurements of recombination at Al contacts. (b) Lifetime mapping of the test sample, measured by MWPCD. The sample consists of 23 areas of 25 × 25 mm on the 156 × 156 cm² wafer. The pitch p varies from 300 to 3500 μm and contact width varies from 80 to 500 μm.

voltage V_{oc} and the maximum attainable efficiency of solar cells. Fig. 7 shows the simulated $j_{0,Al}$ as a function of Al doping depth. The model considers the influence of SRH recombination and Auger recombination, and takes the effect of incomplete ionization of Al acceptors into account.[29–31] In Fig. 7(a), the minority carrier surface recombination velocity of the Al-p$^+$ side S_r has been varied from $S_r = 10^0$ cm s^{-1} to $S_r = 10^8$ cm s^{-1}, assuming the defect density N_t is 9×10^{14} cm^{-3}.[29,32] When the surface is perfectly passivated ($S_r = 10^0$ cm s^{-1}), the saturation current density $j_{0,Al}$ is quite low under 300 fA cm^{-2}. Due to the fact that the defect traps increase in the doped region, the rising trend of $j_{0,Al}$ with the increase of the Al emitter thickness can be seen. Similar trends can also be observed for 2.6×10^3, 8×10^3 and 10^4 cm s^{-1} curves. For $S_r = 1.5 \times 10^4$ cm s^{-1}, the $j_{0,Al}$ characteristics become nearly constant. With increasing S_r values, $j_{0,Al}$ rises quite quickly especially for relatively poorly passivated emitters ($S_r > 1.5 \times 10^4$ cm s^{-1}) at low Al profile depths. The $j_{0,Al}$ profiles decline with the Al-p$^+$ region thickness, and this trend is more significant with the increase of S_r. The reason is that the field passivation effect by preventing the minority carriers to the surface is enhanced for thicker Al-p$^+$ depths, leading to weakened recombination at the surface and a decrease in $j_{0,Al}$.

3.4 Determination of recombination velocity around Al contacts

In order to characterize the surface recombination velocity S_{met} of metallized rear surfaces, we follow the approach presented in ref. 33 and 34, MWPCD measurements were performed to obtain the area-averaged effective rear surface recombination velocity S_{rear} for each single 25 × 25 mm² area in the test wafers. The image of the test sample and the MWPCD lifetime mapping is shown in Fig. 8. For high t_{Bulk} and low surface recombination velocities, the effective carrier lifetime is approximated by[35]

$$\frac{1}{\tau_{\text{eff}}} = \frac{S_{\text{front}} + S_{\text{rear}}}{W}. \tag{2}$$

Fischer's analytical model describes the area averaged effective rear surface recombination velocity,[36] which is a function of the base series resistance R_s, the sample thickness W, the diffusion coefficient D, the metallization area fraction f, the surface recombination velocity in the passivated area S_{pass} as well as the surface recombination velocity under the contact S_{cont}.

$$S_{\text{rear}} = \left(\frac{R_s - \rho W}{\rho D} + \frac{1}{f S_{\text{cont}}} \right)^{-1} + \frac{S_{\text{pass}}}{1 - f}. \tag{3}$$

The R_s depends on the contact layout, and the metallization area fraction f. For line contacts, the metallization area fraction $f_{\text{line}} = \dfrac{a}{p}$ depends on the line widths a and the contact pitches p. The R_s is calculated according to ref. 37:

$$R_s = \frac{p\rho}{2\pi} \ln \left(\frac{2\left(\sqrt{\cosh \frac{\pi a}{4W}} + 1 \right)}{\sqrt{\cosh \frac{\pi a}{4W}} - 1} \right) + \rho W \left(1 - \exp\left(-\frac{W}{p} \right) \right),$$
$$\tanh \frac{\pi a}{4W} \leq \frac{1}{\sqrt{2}}$$

$$R_s = \frac{p\rho\pi}{2} \left[\ln \left(\frac{2\left(1 + \sqrt{\tanh \frac{\pi a}{4W}} \right)}{1 - \sqrt{\tanh \frac{\pi a}{4W}}} \right) \right]^{-1}$$
$$+ \rho W \left(1 - \exp\left(-\frac{W}{p} \right) \right), \quad \frac{1}{\sqrt{2}} < \tanh \frac{\pi a}{4W} \leq 1. \tag{4}$$

In Fig. 9(a), the dependence of S_{rear} on the respective line pitch in each 25 × 25 mm² area is shown. The red and blue solid squares are S_{rear} calculated from experiments using eqn (2), the red and the blue curves are fitted results. S_{rear} decreases with increasing line pitch due to the decrease in metallization fraction. Applying a SiO$_2$ interface layer and improved Al-p$^+$ conditions results in significantly much lower S_{rear} values
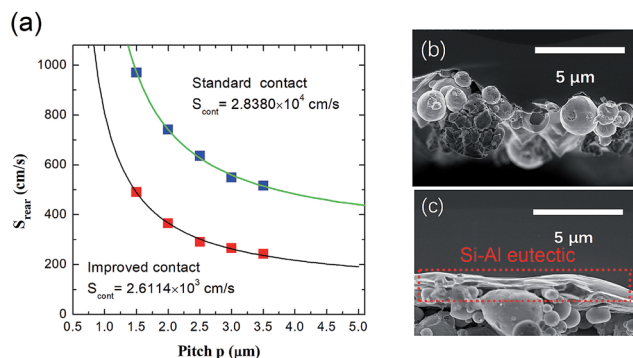
(a)

Fig. 9 (a) Effective rear-surface recombination velocity S_{rear} as a function of line pitch p measured from the samples in (b) and (c). The square symbols correspond to experimental results for contacts prepared by the standard method (blue) and improved method (red). The green and black lines show the fits of the analytical model to the measured data. (b) and (c) SEM images of Si−Al interface of contacts prepared by the standard and improved methods, respectively.
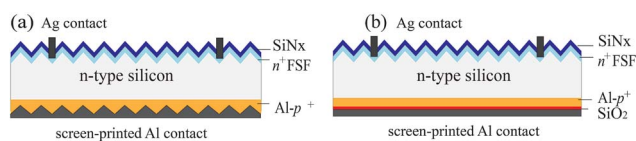

Fig. 10 Schematic of n-type solar cells. The rear Al-p$^+$ emitters are alloyed from screen-printed pastes. (a) Standard solar cell with SiN$_x$ FSF passivation and pyramidally textured rear surface. (b) Improved solar cell with SiN$_x$ FSF passivation, polished rear surface, optimized Al emitter and interfacial oxide layer.

compared to that under the standard industrial condition. By fitting experimental results using eqn (3) and (4), we extract $S_{met} = 2.8380 \times 10^4$ cm s^{-1} for the conventional screen-printed standard contacts and $S_{met} = 2.6114 \times 10^3$ cm s^{-1} for the improved contacts. To understand the change in S_{cont} measured at the two contacts, we investigate the formation of the Al-p$^+$ layer beneath the contacts by means of SEM. The SEM images of contact cross sections are shown in Fig. 9(b) and (c). Analyzing cross-sectional images, the most noticeable finding is a considerably thickened eutectic layer at the interface of Si–Al for the improved contacts. The significant decrease in S_{met} is attributed to the homogeneous Al-p$^+$ region and the thick Si–Al eutectic formation over the entire contact, as indicated by the red dot square in Fig. 9(c). In contrast, the Si–Al interface using the standard method exhibits inadequate contact between the

Si bulk and the metal, no continuous Si–Al eutectic is observed in Fig. 9(b).

3.5 Determination of the specific resistance

In order to achieve good electrical properties of solar cells, one of the primary conditions is to form a low-resistance ohmic contact between Si and Al. To study series resistance in our solar cells, their interface influence is tested by Suns-V_{oc} measurements[38] and light I–V measurements. The cells structures under test are shown in Fig. 10. According to eqn (5), the difference between PFF and FF translates into a series resistance of $R_{s,\text{Suns-}V_{oc}}$[39,40]

$$R_{s,\text{Suns-}V_{oc}} = (\text{PFF} - \text{FF}) \frac{V_{oc} J_{sc}}{J_{mpp}^2}. \tag{5}$$

The FF is the fill factor from I–V curves and PFF is the pseudo fill factor from Suns-V_{oc} curve, J_{sc} and J_{mpp} are short-circuit current density and current density at the maximum power point, respectively. It is calculated to be 0.94 ± 0.28 mΩ for the improved samples and 2.12 ± 0.71 mΩ for the standard samples. A decrease of 1.18 mW is realized. The smaller $R_{s,\text{Suns-}V_{oc}}$ values of group 2 cells is due to the thickened and uniform Si–Al alloy layer, which enables better transport of the majority carriers.

3.6 Solar cells

We applied the improved Al emitter to the 156×156 mm^2 large-area back junction solar cells. The schematic solar cell structures are shown in Fig. 10. The standard solar cells (group 1) were fabricated using the industrial process for reference purposes. We notice that the height of the pyramids on the rear surface cannot be compensated even printing more Al, because the thick Al pastes are not able to completely reach pyramid bottom. For the solar cells in the improved process (group 2), a SiO$_2$ ultra-thin layer is applied to the Si–Al interface at the rear side and the corresponding optimized annealing condition is used. The influence of the polished rear surface has been studied in our previous work.[7] Compared with the cells featuring a polished rear surface without an interfacial layer, further improvements in the electronic parameters due to the SiO$_2$ layer was evidenced.

Table 1 shows the I–V characteristic data of both cell types. An important finding is that the application of the ultra-thin SiO$_2$ layer does not hinder the majority charge carrier transport across its barrier and thus allows for good FF of 79.82% and pFF of 80.6%. The reduced R_s and $R_{s,\text{Suns-}V_{oc}}$ for group 2

Table 1 Solar cell parameters measured under standard testing conditions (AM1.5, 1000 W m^{-2}, 25 °C). The average values are calculated from 4–10 cells

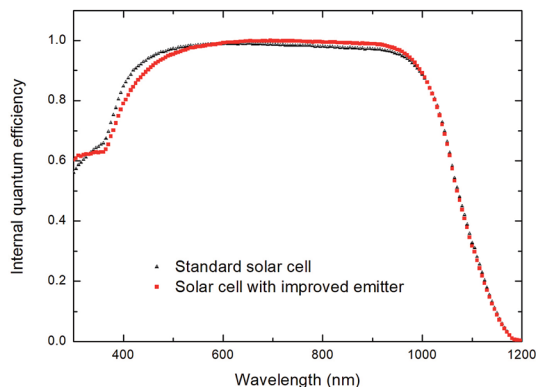| Cell groups	V_{oc} (mV)	J_{sc} (mA cm^{-2})	R_s (mΩ)	FF (%)	Eff. (%)	PFF (%)	$R_{s,\text{Suns-}V_{oc}}$ (mΩ)
1 Average	623.20 ± 9.85	35.97 ± 0.53	3.00 ± 1.78	72.71 ± 3.02	16.32 ± 1.09	80.13 ± 1.03	2.12 ± 0.71
Best	633.30	36.60	1.96	74.69	17.32	80.60	1.92
2 Average	636.03 ± 1.02	36.96 ± 0.31	1.05 ± 0.47	78.68 ± 1.31	18.50 ± 0.41	82.55 ± 0.35	0.94 ± 0.28
Best	637.47	37.59	0.59	79.95	19.16	82.20	0.46

Fig. 11 Internal quantum efficiency curves of the standard solar cell and the solar cell with an optimized emitter.

again stress the importance of the formation of a thick continuous eutectic at the rear contacts. As expected, the average V_{oc} of the solar cells with optimized emitters is greatly increased to 636.03 mV, and J_{sc} is increased to 36.96 mA cm^{-2}. The positive consequences are also apparent from the internal quantum efficiency (IQE) measurement which is shown in Fig. 11. A remarkable high response in the whole spectrum range is observed. We observe slightly lower IQE at short wavelengths for the optimized solar cell, the reason might lie in that the post-annealing process caused damage to the SiN$_x$ FSF passivation layers. However, better responses in long wavelength are clearly due to the optimized Al-p$^+$ region, reduced recombination on the rear surface and in the emitter. The improvement in absolute efficiency is 2.18%, resulting in a 19.16% efficient, fully screen-printed solar cell when compared with solar cells fabricated by the conventional screen-printed process.

4   Conclusion

Al emitters and contacts realized by full-area screen-printing of an Al paste have been intensively investigated. In order to form an optimal Al-p$^+$ region for solar cells, an ultra-thin SiO$_2$ layer at the interface of the metal and silicon was proposed and post-annealing treatments were adopted. A combination of experimental results and model calculations have been used to provide an understanding of the recombination effects in emitter and contacts, the transport properties, and the trends to choose optimal process conditions. It has been shown that the oxide layer acts as a barrier layer, migrating the inhomogeneity of the Al-p$^+$ layer, and improving the morphology around rear contacts. As a result, recombination at the Si–Al interface, in the emitter and around contacts is significantly reduced. We further applied the improved emitters to large-area n-type industrial solar cells (156 × 156 mm^2) with a full-area Al screen-printed rear emitter, gains of average efficiency by 2.18%, the V_{oc} by 12.82 mV, the FF by 5.97% and the J_{sc} by 0.99 mA cm^{-2} were obtained. An optimal cell with an efficiency of 19.16%, V_{oc} 637.47 mV was achieved. Further improvements in cell performance can still be expected if the annealing process is conducted in ambient N$_2$, and by thickness optimization of SiO$_2$.

Conflicts of interest

There are no conflicts to declare.

Acknowledgements

Notes and references

1   H. Hannebauer, T. Dullweber, U. Baumann, T. Falcon and R. Brendel, *Phys. Status Solidi RRL*, 2014, **8**, 675–679.

2   N. Wehmeier, A. Nowack, B. Lim, T. Brendemühl, S. Kajari-Schröder, J. Schmidt, R. Brendel and T. Dullweber, *Sol. Energy Mater. Sol. Cells*, 2016, **158**, 50–54.

3   J. Chen, J. Deckers, P. Choulat, I. Kuzma-Filipek, M. Aleman, A. U. De Castro, Z. R. Du, F. Duerinckx, B. Hoex, J. Szlufcik, J. Poortmans and A. G. Aberle, *Prog. Photovoltaics Res. Appl.*, 2015, **23**, 1706–1714.

4   J. Szlufcik, S. Sivoththaman, J. F. Nijs, R. P. Mertens and R. V. Overstraeten, in *McEvoy's Handbook of Photovoltaics*, ed. S. A. Kalogirou, Academic Press, 3rd edn, 2018, pp. 129–158.

5   M. T. Zarmai, N. N. Ekere, C. F. Oduoza and E. H. Amalu, *Appl. Energy*, 2015, **154**, 173–182.

6   M. Rauer, C. Schmiga, M. Glatthaar and S. W. Glunz, *Sol. Energy Mater. Sol. Cells*, 2018, **176**, 295–301.

7   Y. Wei, P. Li, Y. Wang, X. Tan, C. Song, C. Lu, Z. Zhao and A. Liu, *Sol. Energy*, 2015, **118**, 384–389.

8   M. A. Green, *Sol. Energy*, 2003, **74**, 181–192.

9   S. Singh, F. Dross, N. E. Posthuma and R. Mertens, *Sol. Energy Mater. Sol. Cells*, 2011, **95**, 1151–1156.

10 A. Moehlecke, F. S. Febras and I. Zanesco, *Sol. Energy*, 2013, **96**, 253–262.

11 C. Gong, S. Singh, J. Robbelein, N. Posthuma, E. Van Kerschaver, J. Poortmans and R. Mertens, *Prog. Photovoltaics Res. Appl.*, 2011, **19**, 781–786.

12 R. Woehl, J. Krause, F. Granek and D. Biro, *IEEE Electron Device Lett.*, 2011, **32**, 345–347.

13 X. Xi, X. Chen, S. Zhang, Z. Shi and G. Li, *Appl. Surf. Sci.*, 2015, **339**, 116–121.

14 F. Huster and Others, *Proceedings of the 20th European Photovoltaic Solar Energy Conference*, 2005, pp. 1466–1469.

15 T. Yoshikawa and K. Morita, *J. Electrochem. Soc.*, 2003, **150**, G465.

16 O. Krause, H. Ryssel and P. Pichler, *J. Appl. Phys.*, 2002, **91**, 5645.

17 M. Rauer, C. Schmiga, J. Krause, R. Woehl, M. Hermle and S. W. Glunz, *Energy Procedia*, 2011, **8**, 200–206.

18 J. Krause, R. Woehl, M. Rauer, C. Schmiga, J. Wilde and D. Biro, *Sol. Energy Mater. Sol. Cells*, 2011, **95**, 2151–2160.

19 R. Bock, P. P. Altermatt, J. Schmidt and R. Brendel, *Semicond. Sci. Technol.*, 2010, **25**, 105007.

20 P. A. Basore and B. R. Hansen, *IEEE Conference on Photovoltaic Specialists*, 1990, vol. 1, pp. 374–379.

21 V. Meemongkolkiat, K. Nakayashiki, D. S. Kim, R. Kopecek and A. Rohatgi, *J. Electrochem. Soc.*, 2006, **153**, G53.

22 G. Huster and F. Schubert, *Proceedings of the 20th European Photovoltaic Solar Energy Conference*, 2005, pp. 1462–1465.

23 P. Li, Y. Wei, Z. Zhao, X. Tan, J. Bian, Y. Wang, C. Lu and A. Liu, *Appl. Surf. Sci.*, 2015, **357**, 1830–1835.

24 D. E. Kane and R. M. Swanson, *IEEE photovoltaic specialists conference*, 1985, pp. 578–583.

25 R. Woehl, P. Gundel, J. Krause, K. Ruhle, F. D. Heinz, M. Rauer, C. Schmiga, M. C. Schubert, W. Warta and D. Biro, *IEEE Trans. Electron Devices*, 2011, **58**, 441–447.

26 T. Mankad, R. A. Sinton, J. Swirhun and A. Blum, *Energy Procedia*, 2013, **38**, 137–146.

27 Z. Zhao, P. Li, Y. Wei, C. Lu, X. Tan and A. Liu, *Sol. Energy*, 2014, **110**, 714–719.

28 C. Mader, R. Bock, J. Schmidt and R. Brendel, *Sol. Energy Mater. Sol. Cells*, 2011, **95**, 1720–1722.

29 M. Rüdiger, M. Rauer, C. Schmiga and M. Hermle, *J. Appl. Phys.*, 2011, **110**, 024508.

30 H. Haug and J. Greulich, *Energy Procedia*, 2016, **92**, 60–68.

31 J. Schmidt, N. Thiemann, R. Bock and R. Brendel, *J. Appl. Phys.*, 2009, **106**, 093707.

32 J. Davis, a. Rohatgi, R. Hopkins, P. Blais, P. Rai-Choudhury, J. McCormick and H. Mollenkopf, *IEEE Trans. Electron Devices*, 1980, **27**, 677–687.

33 J. Müller, K. Bothe, S. Gatz, H. Plagwitz, G. Schubert and R. Brendel, *IEEE Trans. Electron Devices*, 2011, **58**, 3239–3245.

34 J. Müller, K. Bothe, S. Gatz, H. Plagwitz, G. Schubert and R. Brendel, *Energy Procedia*, 2011, **8**, 337–342.

35 A. B. Sproul, *J. Appl. Phys.*, 1994, **76**, 2851–2854.

36 B. Fischer, Ph.D. thesis, Universität Konstanz, Fachbereich Physik Konstanz, March 2003.

37 H. Plagwitz, Ph.D. dissertation, Univ. Hanover, 2007.

38 R. A. Sinton and A. Cuevas, *Appl. Phys. Lett.*, 1996, **69**, 2510.

39 F. Feldmann, M. Bivour, C. Reichel, M. Hermle and S. W. Glunz, *Sol. Energy Mater. Sol. Cells*, 2014, **120**, 270–274.

40 D. Pysch, A. Mette and S. W. Glunz, *Sol. Energy Mater. Sol. Cells*, 2007, **91**, 1698–1706.